Hydraulic model calibration using CryoSat-2 observations in the Zambezi catchment

Cécile M. M. Kittel[1], Simbidzayi Hatchard[2], Jeffrey C. Neal[2], Karina Nielsen[3], Paul D. Bates[2], Peter Bauer-Gottwein[1]

[1]Department of Environmental Engineering, Technical University of Denmark, Kgs. Lyngby, Denmark

[2]School of Geography, University of Bristol, Bristol, United Kingdom

[3]National Space Institute, Technical University of Denmark, Kgs. Lyngby, Denmark

Corresponding author: Cécile M. M. Kittel (ceki@env.dtu.dk)

Key Points:

- We use satellite altimetry observations from CryoSat-2 and a steady-state solver to calibrate hydraulic model parameters
- We develop an outlier filtering method for CryoSat-2 observations in ungauged catchments based on rainfall-runoff model simulations
- We integrate the altimetry observations in an efficient global calibration approach at low cost compared to a 1D hydrodynamic model

Abstract

Geodetic altimeters provide unique observations of the river surface longitudinal profile due to their long repeat periods and densely spaced ground tracks. This information is valuable for calibrating hydraulic model parameters, and thus for producing reliable simulations of water level for flood forecasting and river management, particularly in poorly instrumented catchments. In this study, we present an efficient calibration approach for hydraulic models based on a steady-state hydraulic solver and CryoSat-2 observations. In order to ensure that only coherent forcing/observation pairs are considered in the calibration, we first propose an outlier filtering approach for CryoSat-2 observations in data-scarce regions using simulated runoff produced by a hydrologic model. In the hydraulic calibration, a steady-state solver computes the WSE profile along the river for selected discharges corresponding to the days of CryoSat-2 overpass. In synthetic calibration experiments, the global search algorithm generally recovers the true parameter values in portions of the river where observations are available, illustrating the benefit of dense spatial sampling from geodetic altimetry. The most sensitive parameters are the bed elevations. In calibration experiments with real CryoSat-2 data, validation performance against both Sentinel-3 WSE and in-situ records is similar to previous studies, with RMSD ranging from 0.43 to 1.14 m against Sentinel-3 and 0.60 to 0.73 against in-situ WSE observations. Performance remains similar when transferring parameters to a one-dimensional hydrodynamic model. Because the approach is computationally efficient, model parameters can be inverted at high spatial resolution to fully exploit the information contained in geodetic CryoSat-2 altimetry.

1. Introduction

Climate change and human activities have altered river regimes globally, posing significant challenges for water resources managers (Mahé et al., 2013). Flood and drought patterns are changing calling for robust flood hazard and risk assessment. Many river basins are currently ungauged or sparsely gauged (Hannah et al., 2011), as monitoring efforts and data accessibility have severely declined in recent decades (Vörösmarty et al., 2001). However, a reasonable hydraulic representation of river channels is key to producing meaningful large-scale flood models and typically relies on ground monitoring. Simulating river hydraulics at large scale in poorly instrumented regions requires adapted model structures and simplifications to compensate for constraints on computational resources and insufficient ground observations.

Remote sensing observations can be used to retrieve hydraulic parameters and have become a key supplement to in-situ observations in hydrological studies. When parameters cannot be sensed remotely, calibration is a key step to ensure the simulated quantities agree with observations of the system (Michailovsky et al., 2012). Thus bathymetry and channel roughness still need to be estimated through calibration or assumptions made by the modeler, e.g. regarding channel geometry (Alsdorf et al., 2007). Methods to achieve this efficiently in data poor regions are greatly needed.

Satellite radar altimeters can measure the water surface elevation (WSE) of inland water bodies, which can be used as an alternative to in-situ level observations. WSE from satellite radar altimetry has been used increasingly in hydrodynamic model calibration studies as a supplement to in-situ gauge data (Paiva et al., 2013; Schneider et al., 2018b) or even as a possible surrogate in ungauged basins (Getirana et al., 2013; Jiang et al., 2019; Liu et al., 2015). Dense water level profiles have been proven useful in the estimation of distributed hydraulic parameters (O'Loughlin et al., 2013; Paris et al., 2016; Schumann et al., 2010). In order to capture small-scale variability of river morphology the spatial sampling must be denser than what can be achieved with short-repeat missions (down to 52 km at the Equator for the two Sentinel-3 satellites). In that respect, geodetic altimeters such as CryoSat-2 provide the opportunity to extract longitudinal profiles of rivers.

Although not designed for hydrological applications, the benefit of high spatial sampling density of geodetic missions for hydraulic studies has been proven in recent years (Jiang et al., 2019; Schneider et al., 2018a, 2018b; Tourian et al., 2016). Schneider et al. (2018) exploited the dense spatial sampling of CryoSat-2 to calibrate channel roughness in the well-gauged Po River at a finer spatial resolution. They compared using homogenous roughness

parameters increasing the spatial resolution from subreach level to 10 km-long sections. The RMSE (Root Mean Square Error) against in-situ observations improved by up to 29 cm. They showed a strong correlation between the channel sinuosity and the spatially variable calibrated channel roughness. Jiang et al. (2019) showed that missions with high spatial coverage, such as CryoSat-2, improved the RMSE against ground observations by up to 4 cm compared to missions with wider ground track spacing such as Envisat or Jason-2 and 3, and that the sharpness of the parameter estimates increased with the ground-track spacing. Tourian et al. (2016) reached a similar conclusion in a study on spatiotemporal densification of altimetry over rivers. The quality of time series at virtual stations deteriorated slightly when including CryoSat-2 data due to assumptions pertaining to the spatial interpolation. However, CryoSat-2 decreased the bias by increasing the spatial representation of the river profile.

An important step in using satellite altimetry for inland water applications is the outlier filtering. Typically, outliers are removed using secondary datasets such as a Digital Elevation Model (DEM) or binary water/land masks (Jiang et al., 2017; Schneider et al., 2017; Schwatke et al., 2015) or by evaluating the observations themselves, e.g. the return waveforms or the backscatter coefficients (e.g. Boergens et al., 2017; Dinardo et al., 2018; Schwatke et al., 2015; Zhang et al., 2020). For larger water bodies or short return missions, statistical outlier removal can be used to further refine the filtering (e.g. Nielsen et al., 2015; Schwatke et al., 2015; Zhang et al., 2020). For medium-sized rivers, the number of observations per ground track may be too low to perform meaningful statistical outlier removal and when bathymetry is unknown, WSE is dominated by the unknown bed elevation and errors larger than 1 m may be difficult to detect. This poses a challenge particularly for geodetic missions, where the seasonal signal cannot be removed. The dense spatial sampling pattern is impractical for on-ground validation and comparison to traditional gauging stations would require aggregation of the observations at the expense of the valuable spatial resolution. Therefore, robust outlier removal procedures are needed to extract useful observations from geodetic altimetry datasets.

Water levels alone can only provide limited information, and the modelling and calibration problems must be adequately formulated to reflect the available observations. Getirana et al. (2013) and Liu et al. (2015) achieve good simulation results when calibrating channel roughness and bed elevation parameters simultaneously in spite of model equifinality. Jiang et al. (2019) investigated the information contained in altimetry WSE and the capability to recover parameter values (bed elevation, channel roughness and channel geometry) through calibration. Only the bed elevation could be consistently retrieved in combination with one of the other parameters. To avoid ambiguity, channel geometry can be inferred e.g. by assuming rectangular river cross-sections (Biancamaria et al., 2009; Jiang et al., 2019) or power channel shapes (Neal et al., 2015) and information from satellite imagery and global databases.

The inverse problem to determine hydrodynamic model parameters is highly non-linear and non-convex. Studies have used local iterative search algorithms such as Levenberg-Marquardt (Jiang et al., 2019; Schneider et al., 2018b) or global search algorithms (Getirana et al., 2013; Liu et al., 2015) to identify the optimal parameters. Global search algorithms are less sensitive to the starting point for non-convex problems; however, a higher number of simulations are usually required to search the parameter space adequately. The computational requirements to calibrate spatially distributed hydraulic parameters constrains the integration of the dataset with model calibration. Solving the shallow water equations – even with efficient solvers – still requires long simulation time, including warm-up periods (Neal et al., 2012). In particular, the benefit of the spatially dense sampling by CryoSat-2 comes at the cost of a low temporal resolution, and the river profile is sampled over an extended period of time. Therefore, efficient calibration approaches balancing parameter accuracy and resources requirements for long observation periods are greatly needed.

In this study, we evaluate how using a steady-state solver of the shallow water equations and a global search algorithm improves the calibration efficiency of hydraulic parameters against robustly selected CryoSat-2 observations. Specifically, we

- Propose an outlier filtering method for CryoSat-2 observations suited for data-scarce regions based on runoff simulations
- Evaluate the capability of retrieving spatially distributed parameter values (i.e. channel roughness and bed elevation at least every 20 km) using a steady-state solution of the Saint-Venant equations and CryoSat-2 observation density in synthetic calibration experiments
- Evaluate the method using real-world CryoSat-2 observations and the steady-state solver in the Zambezi catchment
- Assess the performance cost of transferring the calibrated parameters into a 1D LISFLOOD-FP hydrodynamic model of the Zambezi and evaluate performance against Sentinel-3 water level and in-situ gauge data

2. Data and methods

2.1. Study area

The Zambezi is located in Southern Africa and is the fourth largest river in Africa. It is 2,574 km long and drains a 1.4 million km^2 basin. Precipitation follows a declining North-to-South gradient, with an average of 1,500 mm in the North and 500 mm in the South. The wet season is between October and March. Flow is driven largely by the precipitation climatology but also by retention in large swamps and floodplains, and artificial reservoirs in the basin. The Zambezi provides key ecosystem services, supporting large populations of fauna and flora, but is also an important resource for the people living in the basin. We select three regions within the Zambezi as study areas: the Kafue, the Luangwa and the Upper Zambezi, upstream of the Barotse floodplain, specifically the tributaries Kabompo and Lungwebungo (**Figure 1**).

2.2. Hydrologic model

2.2.1. Rainfall-runoff model

The hydrodynamic model is forced with runoff from a conceptual rainfall-runoff model of the Zambezi basin. The rainfall-runoff model is described in Kittel et al. (2018) and is based on the work by Zhang et al. (2008) who extended the Budyko framework's concept of limits to monthly and daily time steps. The model builds on a representation of the water balance through demand and supply at various levels. At each time step, Fu's representation of the Budyko curve (Zhang et al., 2008) is used to partition precipitation into catchment retention and runoff, and catchment retention into evapotranspiration, groundwater recharge and root-zone storage. The model is coupled to a Nash cascade of linear reservoirs simulating tributary processes.

2.2.2. River delineation and model calibration

The river network is delineated using TauDEM v. 5 (Tarboton, 2015) and the MERIT DEM (Multi-Error-Removed Improved-Terrain Digital Elevation Model, Yamakazi et al., 2017). The model is forced using GPM (Global Precipitation Model) precipitation (Huffman et al., 2014) and ECMWF ERA-Interim (European Centre for Medium range Weather Forecasts - Interim Reanalysis) (Berrisford et al., 2011) temperature observations for the period 2001 to August 2019. The model is calibrated against in-situ discharge records from 1990-present after careful analysis to ensure hydrometeorological stationarity can be assumed between the observation and simulation periods. In order to parametrize ungauged subcatchments, the subcatchments were grouped into calibration clusters using the European Space Agency Climate Change Initiative Land Cover map v.2 (ESA, 2017) and the MERIT DEM and calibrated holistically using an aggregated objective function at catchment scale allowing trade-offs between parameters in nested subcatchments. The model setup and performance is summarized in Appendix A and B. The parameter regionalization approach and calibration methods are described in Kittel et al. (2020a).

2.3. Radar Altimetry

2.3.1. CryoSat-2

CryoSat-2 Level 2 data were provided by the National Space Institute, Technical University of Denmark (DTU Space) for the period 16-07-2010 to 21-03-2018. The data is based on the 20Hz Level-1b ESA dataset and has been retracked at DTU Space using an empirical retracker based on a sub-waveform threshold (Villadsen et al., 2016). In the Zambezi, CryoSat-2 operates only in Low Resolution Mode (LRM). The DEM and CryoSat-2 observations are reprojected onto the EGM2008 using VDatum (Myers et al., 2007).
First, we use the water occurrence maps from Pekel et al., (2016) to extract observations over the river. We use a threshold of 10% water occurrence frequency, and allow a 90-m buffer zone around the river mask based on the results from Schneider et al., (2018). The footprint in LRM is several km wide (2.5 km^2 with a diameter of 1.64 km)

and a return signal from the water surface can be captured before and after the satellite has crossed the river. Parabolic distortions of the water levels due to this so-called "hooking effect" (Frappart et al., 2006; Maillard et al., 2015), are expected to be negligible at the scale of the buffer applied.
Second, we remove observations deviating from the local value of the MERIT DEM by more than 30 m. This ensures that the surface elevation is indeed within the 60 m satellite reception window. In total, CryoSat-2 crossed the Zambezi basin 3,724 times during the observation period, resulting in 291,287 observations over water bodies in the basin. Of those, 38,697 observations are over the river network itself. The rejection rate in step one is 10.5%, yielding 34,647 observations after this step.
Unlike previous studies, the third step takes into account the river dynamics by using the output of the rainfall-runoff model. We fit a one-dimensional smoothing spline to the CryoSat-2 observations on each river reach. The spline curve is assumed to represent the mean water level for the days of observation. The expected deviation, Δy, from the mean level, y_{mean}, associated with the simulated discharge, Q, at the time of sensing assuming uniform flow and a wide rectangular channel is estimated using Eq. 1.

$$\Delta y = \left(\left(\frac{Q}{Q_{mean}} \right)^{\frac{3}{5}} - 1 \right) y_{mean} \qquad (1)$$

We calculate the mean discharge, Q_{mean}, using only the days with CryoSat-2 observations. We use error propagation to estimate the total uncertainty of Δy based on assumed uncertainties of the discharge estimate, width, slope and Manning's number (**Table 1**). By applying a range of smoothing factors in the spline interpolation of WSE, we obtain different estimates of the deviation from the mean water level (Δy) for each CryoSat-2 observation. If the deviation falls outside of the predicted confidence interval of Δy for all smoothing factors the observation is rejected.

Table 1 Assumed uncertainties of parameters used to estimate the confidence interval of the WSE deviation Δy

Parameter	Estimate	Error propagation
Q	Daily discharge from rainfall-runoff model	+/- 25 %
Slope	From univariate spline function (minimum fixed at 10^{-5})	2 x standard deviation over the reach
Manning's n	0.035	Calibration range: 0.02-0.05
Width	GRWD database	+/- 25 %

The effect of the spline function smoothing factor on the magnitude of the level deviation from the mean is mitigated by using an ensemble of spline curves using varying smoothing factors (0.01-4 times the number of observations in the reach).

2.3.2. Sentinel-3

The Sentinel-3 dataset is independent of the data used to calibrate the steady-state model and its virtual stations' monitoring network is denser and with more recent observations than the ground network. Sentinel-3 Level-2 WSE observations were obtained from the ESA GPOD (Grid Processing on Demand SAR Versatile Altimetric Toolkit for Ocean Research and Exploitation) service (available on https://gpod.eo.esa.int/). The data has been described and evaluated in Kittel et al. (2020b).

2.4. In-situ observations

In situ observations were available for five subcatchments in the Upper Zambezi and in the Kafue, and two out of 12 subcatchments in the Luangwa (Appendix A). The Zambezi River Authority (ZRA) kindly provided in-situ observations in the Upper Zambezi, completing the dataset from Michailovsky & Bauer-Gottwein (2014). In-situ discharge was used for the calibration of the rainfall-runoff model, while in-situ stage at two stations (Kabompo and Chavuma) was used to validate the hydraulic model. To avoid bias related to the vertical datum of the datasets, all records are referenced to their long-term mean and only amplitudes are compared.

2.5. Steady-state solver

2.5.1. Saint-Venant equations

The steady-state solver is based on the Saint-Venant equations, which express the mass balance and momentum balance equations for gradually varied one-dimensional flow in an open channel

$$\frac{\partial A}{dt} + \frac{dQ}{dx} = q \qquad (2)$$

$$\frac{\partial Q}{\partial t} + \frac{\partial}{\partial x}\left(\frac{\beta Q^2}{A}\right) + gA\frac{\partial h}{\partial x} - gA\left(S_0 - S_f\right) = 0 \qquad (3)$$

x is the chainage or distance along the channel [m], t the time [s], h the channel depth [m], Q the discharge [m^3/s], A, the flow cross-sectional area [m^2], q the lateral inflow [m^3/s], g, the acceleration due to gravity (set to 9.81 m^2/s) and β the momentum coefficient (set to unity). The bed slope, S_0 [m/m] is given by

$$S_0 = -\frac{dz}{dx} \qquad (4)$$

z is the channel datum or bed elevation above a given height. The friction slope, S_f [m/m], is given by

$$S_f = \frac{Q^2}{K^2} \qquad (5)$$

K, the conveyance [m^3/s], can be expressed as a function of channel cross-section geometry using Manning's equation

$$K = \frac{A^{\frac{5}{3}}}{n \times P^{\frac{2}{3}}} \qquad (6)$$

P is the wetted perimeter [m] and n is Manning's friction coefficient [$s/m^{1/3}$]. The derivation of the equations for the steady-state solver is detailed in Appendix C.
Equation 7 is the general form of the equation to solve, when assuming steady flow (i.e. constant discharge over time) and lateral inflow in a rectangular channel, where RHS (Right Hand Side) is the collection of terms not containing the derivative of the depth with respect to the chainage

$$\frac{dh}{dx} = \frac{\left(\frac{Q^2}{gA^3}\frac{\partial A}{\partial x} + S_0 - \frac{Q^2}{K^2} + \frac{2Q \times q}{gA^2}\right)}{\left(1 - \frac{Q^2}{gA^3}\frac{\partial A}{\partial h}\right)}$$

$$\frac{dh}{dx} = RHS\left(x, h(x)\right) \qquad (7)$$

Where q is the lateral inflow at chainage x. Lateral inflow consists of runoff generated by the rainfall-runoff model in tributary subcatchments, which enters the hydrodynamic model at the most upstream node, and runoff produced in the subcatchment itself, which is distributed along the chainage proportionally to the contributing area.
The solver is initialized by calculating the downstream water level boundary condition using Manning's equation and a downstream slope of $2e^{-4}$ m/m at chainage, i. The level is then calculated stepwise at Δx spatial increments, moving upstream along the channel and solving Eq. 10 either implicitly (Eq. 11) or explicitly (Eq. 12):

$$h_{i-1} = h_i - \frac{1}{2} \times \left(RHS(x_i, h_i) + RHS(x_{i-1}, h_{i-1})\right) \times \Delta x \qquad (8)$$

$$h_{i-1} = h_i - RHS(x_i, h_i) \times \Delta x \qquad (9)$$

The explicit solution is faster but requires smaller steps Δx to be stable, while the implicit solution is less sensitive to the spatial increments but requires the solution of a non-linear implicit equation for h_{i-1} at each time step. We tested the speed of the two solvers using a hypothetical formulation of the Kabompo reach channel. The solutions are virtually identical when solving the equations for steps of less than 500 m. The implicit solver runs in 5.3 seconds, whereas the explicit solution needs 0.06 seconds. Even when applying the implicit solution only to cross-sections with observations, the fastest computational time remains slower (0.17 seconds), and the large spatial increments affect the final solution. We therefore use the explicit solver using 250 m spatial steps. If the solution becomes numerically unstable, the spatial step is subdivided into 1 m increments.

2.5.2. Global search algorithm and performance statistics

We define calibration cross-sections every 20 km and at each CryoSat-2 observation. Although the steady-state solver is less computationally demanding than a full hydrodynamic calibration, the number of model parameters must still be constrained. Increasing the parameter space increases the risk of parameter correlation. We therefore remove cross-sections less than 5 km apart for shorter reaches (Kabompo and Upper Zambezi) and 10 km apart for longer reaches (Lungwebungo, Kafue and Luangwa).
The bed elevation and channel roughness are calibrated for each cross-section using the Shuffled Complex Evolution algorithm from the University of Arizona (SCEUA) developed by Duan et al., (1992) and implemented in Python using SPOTPY (Houska et al., 2015). The algorithm uses "complexes" to sample the parameter space. The complexes are evolved independently and shuffled after each evolution cycle to ensure an efficient global search. The number of complexes is the most important parameter in the algorithm setup (Madsen, 2000).
The calibration objective function consists of a data misfit term comparing the residuals between the CryoSat-2 WSE and the simulated WSE

$$E_i = (w_i + z_i) - WSE_{C2,i} \qquad (10)$$

and a smoothness preference for the two parameters along the chainage

$$P_i = \frac{\sqrt{(p_i - p_{i-1})^2}}{f_{smooth}} \qquad (11)$$

f_{smooth} is the smoothness preference: smaller values will give higher weight to P and force the solver to move towards a smoother solution with less abrupt changes in bed elevation or channel roughness.
The calibration objective is

$$Obj = \sqrt{\frac{1}{2N}\left(\sum_{i=1}^{N} E_i^2 + \sum_{i=1}^{N} P_i^2\right)} \qquad (12)$$

The smoothness preference must be chosen to balance a realistic water surface and allowing features from the bed and channel roughness to be simulated. The preference is set to 1, giving equal weight to the smoothness and error objectives due to the types of parameters evaluated. This balances the difference in magnitude between the objectives while still prioritizing a good fit between data and observation.
We compute three additional diagnostic performance measures to evaluate the post-calibration performance of the hydraulic model: the Pearson correlation coefficient, the rank correlation coefficient and the non-parametric Kling-Gupta Efficiency (Pool et al., 2018). The Kling-Gupta Efficiency (KGE) combines the Pearson correlation coefficient, and the biases between mean and observed mean discharge and between the simulated and observed standard deviation. In the non-parametric version, Spearman's rank correlation is used instead and the discharge variability performance is computed using the flow duration curve. The method is less sensitive to assumptions of data linearity, data normality and outliers.

2.5.3. Synthetic experiment and global search algorithm

Synthetic calibration experiments are used to evaluate the capabilities of the steady-state solver and calibration algorithm to retrieve the bed elevation and channel roughness using CryoSat-2-type observations of WSE. We generate a synthetic set of parameters (i.e. bed elevation and Manning's n at all cross-sections) to produce synthetic CryoSat-2 observations in the Kabompo reach, i.e. a synthetic representation of the true WSE. To reflect data uncertainties, the synthetic truth is perturbed with normally distributed random noise with varying standard deviations. Two calibration runs with 10 and 20 complexes, respectively, are performed. The resulting six experiments are:

- 3 cm standard deviation representing in-situ water level accuracy using a) 10 complexes and b) 20 complexes
- 20 cm standard deviation representing high accuracy for altimetry WSE using a) 10 complexes and b) 20 complexes
- 40 cm standard deviation representing average accuracy for altimetry WSE using a) 10 complexes and b) 20 complexes

Parameter sensitivity is evaluated by conducting an extended Fourier amplitude sensitivity test (FAST) (Saltelli et al., 1999) as implemented in SPOTPY (Houska et al., 2015). We compare the total sensitivity of the bed elevation and channel roughness at each cross-section to assess the spatial sensitivity of the two parameters along the river chainage. Over 686.000 model runs are performed to adequately sample the parameter space.

2.5.4. Calibration against real-world observations

We then use the real-world CryoSat-2 observations and calibrate the bed elevation and channel roughness in five reaches in the Zambezi catchment. To ensure that the steady-state assumption is reasonable, we choose CryoSat-2 observations where the 10-day discharge gradient is less than 5% of the mean discharge. This is the case for 69.9% of the CryoSat-2 observations. Furthermore, we classify the simulated runoff and CryoSat-2 observations based on the runoff histogram and time of observation. This ensures that extreme runoff simulations are not given excessive weight during the calibration, assuming that each CryoSat-2 river surface profile is representative of its respective discharge class during calibration.

2.6. LISFLOOD-FP hydrodynamic model

LISFLOOD-FP is a coupled 1D/2D hydrodynamic model simulating the propagation of flood waves along channels (in 1D) and over floodplains (in 2D). LISFLOOD-FP has three solvers available for calculating channel flow. The kinematic wave routing model only considers the friction slope, assuming local and convective acceleration and the free surface gradient are negligible. The diffusive wave model includes an additional pressure term. The sub-grid channel solves the full shallow water equations with the exception of the convective acceleration term (Neal et al., 2012). All three formulations are numerically stable (De Almeida et al., 2012). The model is specifically designed for poorly gauged catchments and has been implemented for a number of sites including the Niger River (Neal et al., 2012), the Congo (O'Loughlin et al., 2020), and rivers in the UK (Sosa et al., 2020).
We use LISFLOOD-FP to simulate the channel hydrodynamics in the transient state. The model requires information about channel geometry in the form of channel slope, channel width and bankfull depth from a DEM or surveyed cross-sections. The bankfull depth is derived from the MERIT DEM, the width from the GRWD database and the bed elevation and channel roughness from the calibrated steady-state solver. The resolution of the input files is 900 m instead of the 250 m used by the steady-state solver to ensure reasonable computation time. The model is forced with daily discharge from headwater catchments and lateral inflow, both simulated by the rainfall-runoff model. To ensure that runoff is allocated realistically, it is distributed according to the contributing area to each channel pixel, obtained from the river delineation. The model is run in 1D as a means to compare the steady-state solver to a transient solver by burning in the channel bed elevation into the DEM.

3. Results

3.1. CryoSat-2 outliers filtering

Figure 2 illustrates the CryoSat-2 river longitudinal profiles and outlier filtering for each of the five reaches. Observations are considered outliers if there is a discrepancy between the seasonality (high or low flow) and the sign of the difference between the data points and the spline function (positive or negative deviation from the mean) or if the magnitude of the difference is unlikely. For instance, in the downstream part of the Upper Zambezi, water level increases of 5 m are unlikely; therefore, the associated CryoSat-2 observations are rejected. The rejection rate is between 10% for Lungwebungo and 24% for Luangwa.

The main challenges in terms of outlier-filtering is adequately fitting the spline function so it is representative of the mean water surface profile along the river line. In the Upper Zambezi, Kafue and Kabompo we removed observations deviating from the spline function by more than twice the residual standard deviation and fitted a new spline function through the remaining observations, resulting in rejection rates of 18%, 19% and 23% respectively. This was necessary due to the combination of large variations in WSE and changes in the reach slope. There is a fine balance between overfitting outliers and smoothing the mean water level.

The Luangwa River runs from North-East to South-West. CryoSat-2 predominantly crosses the Luangwa between March and end of November, thus missing the wet season. Therefore, the CryoSat-2 observations are expected to be relatively close to the mean water elevation with very small predicted residuals. In this case the outlier filtering is particularly sensitive to the estimation of the mean water surface profile. However, reducing the smoothing factors of the spline curve ensemble also increased the risk of admitting clear outliers.

3.2. Synthetic test

The synthetic tests evaluate the impact of observation uncertainties by using respectively 3 cm, 20 cm and 40 cm standard deviations to perturb the synthetic CryoSat-2 observations, and of the number of complexes in the optimization algorithm by evolving 20 complexes instead of the standard 10. The results are shown in **Figure 3**. A larger difference in performance is seen when increasing the observation uncertainty compared to increasing the number of complexes, as seen in the performance statistics (**Table 2**) and the spread in the scatter plot in **Figure 3**. The RMSD is in the order of magnitude of the observation uncertainty. For all uncertainties parameter retrieval is most improved at gauged cross-sections. This was expected and confirms the advantage of using spatially dense observations to calibrate hydrodynamic parameters. The weighted objective used in calibration includes a smoothness factor. There is good consistency between the RMSD and calibration objective, with the smoothness factor forcing a reduction in variations where the observation density is low. Increasing the number of complexes comes at a higher computational cost, and the benefit is limited in terms of calibration objective and parameter retrieval.

Table 2 Calibration performance for the synthetic experiments

Observation uncertainty	σ = 40 cm		σ = 20 cm		σ = 3 cm	
Number of complexes	10	20	10	20	10	20
WSE objective	0.26	0.26	0.15	0.15	0.09	0.09
RMSD [m]	0.33	0.33	0.18	0.17	0.08	0.08
Datum offset RMSD [m]	0.70	0.75	0.60	0.49	0.42	0.56
- at gauged cross-section	0.57	0.53	0.41	0.39	0.38	0.39
Manning's n RMSD [$s/m^{1/3}$]	0.0082	0.0083	0.0088	0.0072	0.0071	0.0075

The downstream sections are most sensitive during calibration according to the FAST sensitivity analysis. The Saint-Venant equations account for backwater effects; therefore, changes in downstream parametrization have an impact on all upstream evaluation points. Tweaking upstream parameters will mainly impact the upstream

predictions in the steady-state solver and thus have limited effect on the overall performance. Sensitivity is driven by the observation density, as seen for the parameters at cross-section 12, which correspond to the first large gap in observations, and are not sensitive at all (**Figure 3** and **Figure 4**).

The analysis also confirms that the objective function is less sensitive to the channel roughness, n, than the datum offset, z, as shown in **Figure 4** (top). The scatter plots in **Figure 4** provide information on whether trade-offs during calibration can explain the low sensitivity of the channel roughness. We plot the results of the low uncertainty calibration, to remove the effect of observation uncertainty on the parameter retrieval. During calibration, the parameters converge to relatively narrow parameter space. The synthetic truth is not always within the optimum range, which is due to the global objective function and trade-offs between parameters at the different cross-sections.

The bed elevation and channel roughness have similar local effects: overestimating the channel roughness raises the water level, but can be compensated by slightly decreasing the bed elevation locally. Previous studies have shown that the two parameters impact the water surface differently over different characteristic spatial scales (Durand et al., 2014; Wood et al., 2016). When calibrating a single, global roughness parameter, the bed elevation will tend to have a local impact, whereas adjustments of the friction parameter will have a more diffuse effect and impact a longer portion of the reach. Thus, the two parameters can be retrieved simultaneously. In this study, both parameters are calibrated locally and both have a local impact. This can be seen at cross-section 0, where the best performing parameter samples (objective function less than 0.2) form a straight line towards the synthetic truth. Thus, although parameters can be retrieved successfully at some cross-sections, there is still model ambiguity (e.g. at cross-section 4). The ambiguity can be partially resolved by increasing the observation density.

3.3. Calibration using real-world CryoSat-2 observations in the Zambezi

Figure 5 shows the calibrated longitudinal water surface profiles at the five locations in the Zambezi after calibrating the steady-state solver against real-world CryoSat-2 observations. Overall, the simulated WSE corresponds quite well to the CryoSat-2 observations.

LISFLOOD-FP models are run for each reach using the calibrated channel roughness and bed elevation. **Table 3** summarizes performance statistics of the calibration and evaluation based on the steady-state solver and the transient solution respectively. We compare the simulated and observed water level by subtracting calibrated bed elevation from the satellite altimetry WSE. This removes the otherwise dominating effect of elevation on the performance. Overall performance is good and consistent across performance metrics. The weighted objective includes a smoothness and shallowness preference and is therefore generally larger than the RMSD. There is a good correlation between the simulated WSE and CryoSat-2 WSE. The RMSD is between 0.58 m and 0.88 m.

Figure 6 shows the WSE time series simulated by LISFLOOD-FP against the in-situ records at Chavuma and Watopa and against the Sentinel-3 WSE. We note that there are some timing issues in the water level prediction, particularly at Chavuma, and in the low flow predictions at Watopa. These are consistent with uncertainties in the rainfall-runoff model, which forces the steady-state hydraulic model and hydrodynamic models. Sentinel-3 is a SAR altimeter and expected to have a lower uncertainty than a conventional altimeter (3-30 cm in the Zambezi, according to Kittel et al., 2020b). We represent the Sentinel-3 data with a slightly higher uncertainty, as the stations used in this study could not all be evaluated against in-situ observations. An upper bound of 50 cm was therefore selected to indicate the Sentinel-3 uncertainty in **Figure 6**.

The steady-state and transient solutions differ by around 20 to 40 cm in RMSD against CryoSat-2 observations, which is in the order of magnitude of the expected CryoSat-2 uncertainty in LRM (Villadsen et al., 2016). The difference between the steady-state and transient solution (22 cm to 98 cm) can be partly explained by 1) the difference between the subgrid representation of the channel and the 1-dimensional line representation of the steady-state solver and 2) the coarser spatial resolution (900 m instead of 250 m) needed to allow reasonable computation time. The performance metrics remain comparable or better than results reported in previous studies.

Table 3 Steady-state (SS) solver and LISFLOOD-FP (L) performance statistics using calibrated parametrization and CryoSat-2 observations (CS), Sentinel-3 (S3) WSE and in-situ water level observations. The Pearson and Spearman correlation coefficients are calculated by subtracting the calibrated bed elevation from the CryoSat-2 observations to remove the effect of elevation on

396 the performance. A p-value below 2.5% is considered significant – in all cases the p-value is
397 below the threshold and the correlation is significant.

	Weighted objective	RMSD					Non-parametric KGE		Pearson r^2			Spearman r^2		
Data source	C2		C2		S3	In-situ	C2	In-situ	C2	S3	In-situ	C2	S3	In-situ
Solver	SS	SS vs. L	SS	L	L	L	L	L	L	L	L	L	L	L
Upper Zambezi	0.68	0.39	0.83	0.79	0.71	0.73	0.79	0.25	0.91	0.79	0.84	0.79	0.82	0.92
Lungwebungo	0.78	0.98	0.88	1.31	0.43		0.50		0.37	0.58		0.53	0.58	
Kabompo	0.45	0.32	0.61	0.71	1.14	0.60	0.89	0.49	0.90	0.69	0.90	0.90	0.79	0.90
Kafue	0.74	0.35	0.89	1.05	0.62		0.78		0.85	0.91		0.85	0.90	
Luangwa	0.54	0.17	0.66	0.60	0.99		0.11		0.58	0.43		0.44	0.61	

398
399 Overall, the performance is consistent with previous studies with RMSD values between 0.60 and 1.31 m. Jiang et
400 al. (2019) obtained RMSD between the simulated and altimetry WSE between 0.72 m and 1.6 m, when using
401 various combinations of altimetry datasets, with CryoSat-2 alone giving a calibration performance of 1.28 m.
402 Domeneghetti et al. (2014) obtained a RMSD of around 1 m using Envisat data to calibrate a hydrodynamic model
403 of the Po river. O'Loughlin et al. (2020) achieved RMSD between 0.84 and 2.02 m in the Congo when comparing a
404 large-scale hydraulic model forced with in-situ and simulated discharge. As in this study, the channel depths and
405 friction were calibrated against satellite altimetry WSE observations; however, the study used a global channel
406 friction parameter.

407 # 4. Discussion

408 ## 4.1. CryoSat-2 data selection

409 The CryoSat-2 observations used in the calibration must be accurate and representative of the river WSE. CryoSat-2
410 is not error-free and difficult to validate due to the high spatial sampling but low temporal sampling frequency. In
411 this study, we used hydrological simulations from a calibrated hydrological model to assess the validity of the
412 CryoSat-2 observations. Instead of selecting a fixed threshold to assess the deviation of a given CryoSat-2
413 observation from the local river surface longitudinal profile, we predict the expected range of water level deviation
414 based on the hydrological conditions in the reach at the time of observation.
415 Robust outlier removal is essential but highly challenging in poorly instrumented catchments. By exploiting
416 simulations of discharge, which are already available as input to the hydraulic model, a more refined method was
417 developed in this study. Valid observations may be rejected due to errors in the corresponding simulated discharge.
418 This is likely to occur in poorly gauged catchments, where calibration is constrained by data availability. Retaining
419 these observations may introduce errors in the calibration, as it fits the parameters to produce water levels, which are
420 unlikely to have occurred under the simulated flow conditions.

421 ## 4.2. Model performance

422 The steady-state assumption of the solver is a simplification of the actual hydrodynamic conditions; it can be run for
423 specific time steps corresponding to satellite overpasses greatly reducing computational time. The results are in the
424 order of magnitude of the calibration data uncertainty and comparable to previous studies. This confirms that the
425 method can be used to calibrate hydraulic models efficiently against spatially dense WSE observations.
426 Furthermore, simplifications are necessary to represent poorly instrumented river channels for hydraulic modelling.
427 In particular, some assumption on the cross-section geometry is required (e.g. trapezoidal, rectangular channel,

power channel). In this study, we select a simple rectangular shape, and use global river width databases to obtain the missing information about the mean width. An alternative approach could be to use a power-law to correlate the area and water depth and the conveyance and water depth, removing the need for an explicit definition of the channel shape.

Neal et al. (2015) investigated incorporating the channel cross-section uncertainty into large-scale flood inundation models of data sparse areas and showed that performance improved in models with calibrated channel friction and rectangular channels. Their results suggest that a channel shape parameter, roughness and elevation could be fitted simultaneously, provided sufficient dynamic observations are available in the reach. Neal et al. (2015) also showed that informing the model with even basic information about the channel geomorphology, such as width-discharge curves from optical or radar satellite imagery improved model calibration against level observations. The shape and friction have similar effects locally, and calibrating the shape parameter may be more appropriate than calibrating friction for narrow channels, where the assumption of a rectangular shape is less appropriate.

The calibration of local variations in channel roughness greatly increases the parameter space, and poses a further challenge. Jiang et al. (2019) demonstrated that altimetry alone is insufficient to calibrate geometry parameters as well as a spatially distributed channel roughness. The reason for this is clear: local channel conveyance depends on both the channel roughness and flow area. Thus, there is model ambiguity and additional datasets are required to constrain the increased parameter space (e.g. channel width under known flow conditions). The unknown channel bed elevation prevents a satisfactory calibration of the level to area relationship and channel roughness. Thus, an interesting future path could include exploring whether the geometry parameters could be sufficiently constrained from alternative or new remote sensing observations, or whether calibrating local changes in channel geometry may be more robust than calibrating the channel roughness.

4.3. 1D versus 2D hydrodynamic model

The steady-state solver is one-dimensional and thus does not include bank overflow and floodplain processes. This will introduce errors in shallow reaches during extreme events, where the peak water level might be over-predicted to accommodate the high flow in a rectangular channel. The subgrid solver in LISFLOOD-FP calculates the floodplain water level when the level in the channel exceeds the bank elevation. This requires a robust match between bed and bank elevation. **Figure 7** illustrates the calibrated cross-sections versus the DEM at selected locations of the five reaches. Because the steady-state solver only calibrates the bed elevation, the bank elevation is extracted from the DEM. This poses a challenge if the calibrated bed is equal to or higher than the DEM elevation height, e.g. in the Upper Zambezi (**Figure 7**). The calibration information then becomes obsolete. If the difference is too small, the channel might overflow too often (as might be the case at Kabompo). Thus to apply the results in a 2D modelling setup, the bank elevation must be corrected, to ensure the channel is correctly burnt into the floodplain, e.g. using SAR imagery to deduce the bank and bed elevation relationship (Wood et al., 2016).

The DEM will usually give the elevation of the water surface in the channel at time of observation. This means that the calibrated bed elevation is more likely to be below than above the DEM elevation. The opposite occurs at Chavuma, where the slope is very high. CryoSat-2 observations before and after the drop in elevation force a compromise.

5. Conclusion

A reasonable hydraulic representation of river channels for large-scale flood modeling is essential but challenging to obtain in data poor regions. In this study, we propose using a steady-state solver to calibrate hydraulic parameters against geodetic altimetry observations. We propose an informed outlier rejection framework based on simulated discharge to select CryoSat-2 observations for calibration. The approach successfully removes obvious outliers, while allowing reasonably large deviations from the estimated mean level, provided there is coherence with the hydrological conditions on the day of observation. Furthermore, it ensures that only coherent forcing/observation pairs are included in the calibration. The method enables filtering spatially dense WSE observations from geodetic satellite altimetry missions in data sparse regions, where traditional outlier identification methods fail.

Hydraulic parameter retrieval was evaluated in synthetic experiments, focusing on the impacts of observation density and quality, and on the calibration setup. Bed elevation was retrieved with a RMSD of 42-75 cm and channel roughness with a RMSD of 0.007-0.009 $s/m^{1/3}$. The calibration revealed a higher sensitivity to the elevation offset compared to the roughness parameter, resulting in a poor retrieval of the upstream channel roughness. Furthermore, we noted the effect of the WSE observation density, with the most successful performance occurring in densely

observed segments of the reach. Observation uncertainty affected the retrieval of parameters at ungauged cross-sections, and performance was more similar at gauged cross-sections for the three investigated data quality scenarios.

By carefully selecting observations where the steady-state assumption is reasonable, five reaches of the Zambezi were calibrated with satisfactory model performance using real CryoSat-2 observations. Calibration against real-world CryoSat-2 observations was evaluated using a range of statistical diagnostics to confirm the model behavior and compared to Sentinel-3 and in-situ observations of WSE to evaluate the temporal patterns of WSE in the river channels. The method yielded at least as good performance as past studies at far reduced computational cost and the parameter transfer from the steady-state to the transient solver did not impact performance significantly.

It is clear that geodetic altimetry missions hold valuable information for hydrological studies, particularly in ungauged basins. However, the dense spatial sampling requires careful data selection and comes at a computational cost because, in the hydraulic inversion, WSE must be simulated at all points of observation by the hydraulic forward model. The approach presented in this study integrates the altimetry observations in a fast and efficient, global calibration approach at low cost compared to a 1D hydrodynamic model.

References

Alsdorf, D.E., Rodríguez, E., Lettenmaier, D.P., 2007. Measuring Surface Water From Space. Rev. Geophys. 45, 1–24. https://doi.org/10.1029/2006RG000197.1.INTRODUCTION

Berrisford, P., Dee, D.P., Poli, P., Brugge, R., Fielding, M., Fuentes, M., K\r allberg, P.W., Kobayashi, S., Uppala, S., Simmons, A., 2011. The ERA-Interim archive Version 2.0 23.

Biancamaria, S., Bates, P.D., Boone, A., Mognard, N.M., 2009. Large-scale coupled hydrologic and hydraulic modelling of the Ob river in Siberia. J. Hydrol. 379, 136–150. https://doi.org/10.1016/j.jhydrol.2009.09.054

Boergens, E., Buhl, S., Dettmering, D., Klüppelberg, C., Seitz, F., 2017a. Combination of multi-mission altimetry data along the Mekong River with spatio-temporal kriging. J. Geod. 91, 519–534. https://doi.org/10.1007/s00190-016-0980-z

Boergens, E., Nielsen, K., Andersen, O.B., Dettmering, D., Seitz, F., 2017b. Water levels of the Mekong River Basin based on CryoSat-2 SAR data classification. Hydrol. Earth Syst. Sci. Discuss. 1–22. https://doi.org/10.5194/hess-2017-217

De Almeida, G.A.M., Bates, P., Freer, J.E., Souvignet, M., 2012. Improving the stability of a simple formulation of the shallow water equations for 2-D flood modeling. Water Resour. Res. 48, 1–14. https://doi.org/10.1029/2011WR011570

Dinardo, S., Fenoglio-Marc, L., Buchhaupt, C., Becker, M., Scharroo, R., Joana Fernandes, M., Benveniste, J., 2018. Coastal SAR and PLRM altimetry in German Bight and West Baltic Sea. Adv. Sp. Res. 62, 1371–1404. https://doi.org/10.1016/j.asr.2017.12.018

Domeneghetti, A., Tarpanelli, A., Brocca, L., Barbetta, S., Moramarco, T., Castellarin, A., Brath, A., 2014. The use of remote sensing-derived water surface data for hydraulic model calibration. Remote Sens. Environ. 149, 130–141. https://doi.org/10.1016/j.rse.2014.04.007

Duan, Q., Sorooshian, S., Gupta, V., 1992. Effective and Efficient Global Optimization for Conceptual Rainfall-Runoff Models. Water Resour. Res. 28, 1015–1031.

Durand, M., Neal, J., Rodríguez, E., Andreadis, K.M., Smith, L.C., Yoon, Y., 2014. Estimating reach-averaged discharge for the River Severn from measurements of river water surface elevation and slope. J. Hydrol. 511, 92–104. https://doi.org/10.1016/j.jhydrol.2013.12.050

ESA, 2017. Land Cover CCI Product User Guide Version 2. Tech. Rep.

Frappart, F., Calmant, S., Cauhopé, M., Seyler, F., Cazenave, A., 2006. Preliminary results of ENVISAT RA-2-derived water levels validation over the Amazon basin. Remote Sens. Environ. 100, 252–264. https://doi.org/10.1016/j.rse.2005.10.027

Getirana, A.C.V., Boone, A., Yamazaki, D., Mognard, N., 2013. Automatic parameterization of a flow routing scheme driven by radar altimetry data : Evaluation in the Amazon basin. Water Resour. Res. 49, 614–629. https://doi.org/10.1002/wrcr.20077

Hannah, D.M., Demuth, S., van Lanen, H.A.J., Looser, U., Prudhomme, C., Rees, G., Stahl, K., Tallaksen, L.M., 2011. Large-scale river flow archives: Importance, current status and future needs. Hydrol. Process. 25, 1191–1200. https://doi.org/10.1002/hyp.7794

Houska, T., Kraft, P., Chamorro-Chavez, A., Breuer, L., 2015. SPOTting model parameters using a ready-made python package. PLoS One 10, 1–22. https://doi.org/10.1371/journal.pone.0145180

Huffman, G., Bolvin, D., Braithwaite, D., Hsu, K., Joyce, R., Xie, P., 2014. Integrated Multi-satellitE Retrievals for GPM (IMERG), version 4.4. [WWW Document]. NASA's Precip. Process. Cent. URL ftp://arthurhou.pps.eosdis.nasa.gov/gpmdata/ (accessed 6.10.20).

Jiang, L., Madsen, H., Bauer-Gottwein, P., 2019. Simultaneous calibration of multiple hydrodynamic model parameters using satellite altimetry observations of water surface elevation in the Songhua River. Remote Sens. Environ. 225, 229–247. https://doi.org/10.1016/j.rse.2019.03.014

Jiang, L., Nielsen, K., Andersen, O.B., Bauer-Gottwein, P., 2017. CryoSat-2 radar altimetry for monitoring freshwater resources of China. Remote Sens. Environ. 200, 125–139. https://doi.org/10.1016/j.rse.2017.08.015

Kittel, C.M.M., Jiang, L., Tøttrup, C., Bauer-Gottwein, P., 2020. Sentinel-3 radar altimetry for river monitoring - a catchment-scale evaluation of satellite water surface elevation from Sentinel-3A and Sentinel-3B. Hydrol. Earth Syst. Sci. Discuss. https://doi.org/https://doi.org/10.5194/hess-2020-165

Kittel, C.M.M., Nielsen, K., Tøttrup, C., Bauer-Gottwein, P., 2018. Informing a hydrological model of the Ogooué with multi-mission remote sensing data. Hydrol. Earth Syst. Sci. 22, 1453–1472. https://doi.org/10.5194/hess-22-1453-2018

Kittel, C.M.M.M., Arildsen, A.L., Dybkjær, S., Hansen, E.R., Linde, I., Slott, E., Tøttrup, C., Bauer-Gottwein, P., 2020. Informing hydrological models of poorly gauged river catchments - a parameter regionalization and calibration approach. J. Hydrol. 587, 124999. https://doi.org/10.1016/j.jhydrol.2020.124999

Liu, G., Schwartz, F.W., Tseng, K.-H., Shum, C.K., 2015. Discharge and water-depth estimates for ungauged rivers: Combining hydrologic, hydraulic, and inverse modeling with stage and water-area measurements from satellites. Water Resouces Res. 51, 6017–6035. https://doi.org/10.1002/2015WR017200.A

Madsen, H., 2000. Automatic calibration of a conceptual rainfall–runoff model using multiple objectives. J. Hydrol. 235, 276–288. https://doi.org/10.1016/S0022-1694(00)00279-1

Mahé, G., Lienou, G., Descroix, L., Bamba, F., Paturel, J.E., Laraque, A., Meddi, M., Habaieb, H., Adeaga, O., Dieulin, C., Chahnez Kotti, F., Khomsi, K., 2013. The rivers of Africa:

Witness of climate change and human impact on the environment. Hydrol. Process. 27, 2105–2114. https://doi.org/10.1002/hyp.9813

Maillard, P., Bercher, N., Calmant, S., 2015. New processing approaches on the retrieval of water levels in Envisat and SARAL radar altimetry over rivers: A case study of the São Francisco River, Brazil. Remote Sens. Environ. 156, 226–241. https://doi.org/10.1016/j.rse.2014.09.027

Michailovsky, C.I., Bauer-Gottwein, P., 2014. Operational reservoir inflow forecasting with radar altimetry: the Zambezi case study. Hydrol. Earth Syst. Sci. 18, 997–1007. https://doi.org/10.5194/hess-18-997-2014

Michailovsky, C.I., McEnnis, S., Berry, P. a M., Smith, R., Bauer-Gottwein, P., 2012. River monitoring from satellite radar altimetry in the Zambezi River basin. Hydrol. Earth Syst. Sci. 16, 2181–2192. https://doi.org/10.5194/hess-16-2181-2012

Myers, E., Hess, K., Yang, Z., Xu, J., Wong, A., Doyle, D., Woolard, J., White, S., Le, B., Gill, S., Hovis, G., 2007. VDatum and strategies for national coverage. Ocean. Conf. Rec. https://doi.org/10.1109/OCEANS.2007.4449348

Neal, J., Schumann, G., Bates, P., 2012. A subgrid channel model for simulating river hydraulics and floodplain inundation over large and data sparse areas. Water Resour. Res. 48, 1–16. https://doi.org/10.1029/2012WR012514

Neal, J.C., Odoni, N.A., Trigg, M.A., Freer, J.E., Garcia-Pintado, J., Mason, D.C., Wood, M., Bates, P.D., 2015. Efficient incorporation of channel cross-section geometry uncertainty into regional and global scale flood inundation models. J. Hydrol. 529, 169–183. https://doi.org/10.1016/j.jhydrol.2015.07.026

Nielsen, K., Stenseng, L., Andersen, O.B., Villadsen, H., Knudsen, P., 2015. Validation of CryoSat-2 SAR mode based lake levels. Remote Sens. Environ. 171, 162–170. https://doi.org/10.1016/j.rse.2015.10.023

O'Loughlin, F., Trigg, M.A., Schumann, G.J.P., Bates, P.D., 2013. Hydraulic characterization of the middle reach of the Congo River. Water Resour. Res. 49, 5059–5070. https://doi.org/10.1002/wrcr.20398

O'Loughlin, F.E., Neal, J., Schumann, G.J.P., Beighley, E., Bates, P.D., 2020. A LISFLOOD-FP hydraulic model of the middle reach of the Congo. J. Hydrol. 580, 124203. https://doi.org/10.1016/j.jhydrol.2019.124203

Paiva, R.C.D., Collischonn, W., Bonnet, M.P., De Gonçalves, L.G.G., Calmant, S., Getirana, A., Santos Da Silva, J., 2013. Assimilating in situ and radar altimetry data into a large-scale hydrologic-hydrodynamic model for streamflow forecast in the Amazon. Hydrol. Earth Syst. Sci. 17, 2929–2946. https://doi.org/10.5194/hess-17-2929-2013

Paris, A., Dias de Paiva, R., Santos Da Silva, J., Medeiros Moreira, D., Calmant, S., Garambois, P.-A., Collischonn, W., Bonnet, M.-P., Seyler, F., 2016. Stage-discharge rating curves based on satellite altimetry and modeled discharge in the Amazon basin. Water Resour. Res. 53, 3787–3814. https://doi.org/10.1002/2014WR016618.Received

Pekel, J.-F., Cottam, A., Gorelick, N., Belward, A.S., 2016. High-resolution mapping of global surface water and its long-term changes. Nature 540, 418–422.

https://doi.org/10.1038/nature20584

Pool, S., Vis, M., Seibert, J., 2018. Evaluating model performance: towards a non-parametric variant of the Kling-Gupta efficiency. Hydrol. Sci. J. 63, 1941–1953. https://doi.org/10.1080/02626667.2018.1552002

Saltelli, A., Tarantola, S., Chan, K.P., 1999. A Quantitative Model-Independent Method for Global Sensitivity Analysis of Model Output A Quantitative Model-Independent Method for Global Sensitivity Analysis of Model Output. Technometrics 41, 39–56.

Schneider, R., Godiksen, P.N., Villadsen, H., Madsen, H., Bauer-Gottwein, P., 2017. Application of CryoSat-2 altimetry data for river analysis and modelling. Hydrol. Earth Syst. Sci. 21, 751–764. https://doi.org/10.5194/hess-21-751-2017

Schneider, R., Ridler, M.E., Godiksen, P.N., Madsen, H., Bauer-Gottwein, P., 2018a. A data assimilation system combining CryoSat-2 data and hydrodynamic river models. J. Hydrol. 557, 197–210. https://doi.org/10.1016/j.jhydrol.2017.11.052

Schneider, R., Tarpanelli, A., Nielsen, K., Madsen, H., Bauer-Gottwein, P., 2018b. Evaluation of multi-mode CryoSat-2 altimetry data over the Po River against in situ data and a hydrodynamic model. Adv. Water Resour. 112, 17–26. https://doi.org/10.1016/j.advwatres.2017.11.027

Schumann, G., Di Baldassarre, G., Alsdorf, D., Bates, P.D., 2010. Near real-time flood wave approximation on large rivers from space: Application to the River Po, Italy. Water Resour. Res. 46, 1–8. https://doi.org/10.1029/2008WR007672

Schwatke, C., Dettmering, D., Bosch, W., Seitz, F., 2015. DAHITI - An innovative approach for estimating water level time series over inland waters using multi-mission satellite altimetry. Hydrol. Earth Syst. Sci. 19, 4345–4364. https://doi.org/10.5194/hess-19-4345-2015

Sosa, J., Sampson, C., Smith, A., Neal, J., Bates, P., 2020. A toolbox to quickly prepare flood inundation models for LISFLOOD-FP simulations. Environ. Model. Softw. 123, 104561. https://doi.org/10.1016/j.envsoft.2019.104561

Tarboton, D., 2015. TauDEM Version 5 [WWW Document]. Hydrol. Res. Group, Utah State Univ. URL http://hydrology.usu.edu/taudem/taudem5/documentation.html (accessed 1.1.17).

Tourian, M.J., Tarpanelli, A., Elmi, O., Qin, T., Brocca, L., Moramarco, T., Sneeuw, N., 2016. Spatiotemporal densification of water level time series by multimission satellite altimetry. Water Resour. Res. 52, 613–615. https://doi.org/10.1029/2008WR006912.M

Villadsen, H., Deng, X., Andersen, O.B., Stenseng, L., Nielsen, K., Knudsen, P., 2016. Improved inland water levels from SAR altimetry using novel empirical and physical retrackers. J. Hydrol. 537, 234–247. https://doi.org/10.1016/j.jhydrol.2016.03.051

Vörösmarty, C., Askew, A., Grabs, W., Barry, R.G., Birkett, C., Döll, P., Goodison, B., Hall, A., Jenne, R., Kitaev, L., Landwehr, J., Keeler, M., Leavesley, G., Schaake, J., Strzepek, K., Sundarvel, S.S., Takeuchi, K., Webster, F., 2001. Global water data: A newly endangered species. Eos (Washington. DC). 82, 54–58. https://doi.org/10.1029/01EO00031

Westerberg, I.K., Guerrero, J.L., Younger, P.M., Beven, K.J., Seibert, J., Halldin, S., Freer, J.E., Xu, C.Y., 2011. Calibration of hydrological models using flow-duration curves. Hydrol.

Earth Syst. Sci. 15, 2205–2227. https://doi.org/10.5194/hess-15-2205-2011

Wood, M., Hostache, R., Neal, J., Wagener, T., Giustarini, L., Chini, M., Corato, G., Matgen, P., Bates, P., 2016. Calibration of channel depth and friction parameters in the LISFLOOD-FP hydraulic model using medium-resolution SAR data and identifiability techniques. Hydrol. Earth Syst. Sci. 20, 4983–4997. https://doi.org/10.5194/hess-20-4983-2016

Zhang, L., Potter, N., Hickel, K., Zhang, Y., Shao, Q., 2008. Water balance modeling over variable time scales based on the Budyko framework - Model development and testing. J. Hydrol. 360, 117–131. https://doi.org/10.1016/j.jhydrol.2008.07.021

Zhang, X., Jiang, L., Kittel, C.M.M., Yao, Z., 2020. On the performance of Sentinel-3 altimetry over new reservoirs : Approaches to determine on-board a-priori elevation. Geophys. Res. Lett. 47, 1–11. https://doi.org/10.1029/2020GL088770

Acknowledgments, Samples and Data

The authors wish to thank the Zambezi River Authority (ZRA) for kindly providing the in-situ observations in the Upper Zambezi used to evaluate the WSE simulations. The data can requested from the ZRA for research purposes. The Sentinel-3 data used in this study can be freely processed on and downloaded from the ESA GPOD (Grid Processing on Demand SAR Versatile Altimetric Toolkit for Ocean Research and Exploitation) service (available on https://gpod.eo.esa.int/, last accessed 14/10/2020). The MERIT DEM used as reference elevation and in the river delineation was obtained from http://hydro.iis.u-tokyo.ac.jp/~yamadai/MERIT_DEM/, last accessed 14/10/2020). The rainfall-runoff model source code is open source and part of the GlobWetlands-Africa QGIS Toolbox (available on http://globwetland-africa.org/?wpdmpro=globwetland-toolbox-1-5, last accessed 17/11/2020). LISFLOOD-FP can be requested on http://www.bristol.ac.uk/geography/research/hydrology/models/lisflood/downloads/ (last accessed 17/11/2020). The CryoSat-2 observations and model parameters will be made available on Zenodo and are provided as supplement to this article.

Appendix A – In-situ data used in calibration for the RR-model

Table A. 1 Summary of In-situ stations used to calibrate the hydrologic (discharge records) and validate the hydrodynamic model (stage records) and of the number of CryoSat-2 observations available for calibration of the hydraulic model in the three study areas. The mean annual discharge is over the time of simulation, 2001-2018. *: the discharge record at Kabompo Boma has been manually bias-corrected based on historical records from 1990-1992.

Main river and tributaries	Drainage area [km^2]	Length [km]/ tributary to	Observations	Stations	Time of operation	Mean annual discharge [m^3/s]	CryoSat-2 observations after outlier removal
Zambezi	238,667	468.9	Discharge, stage	Chavuma (1105)	1959-2019	656	140
					1990-2006	911	
				Zambezi Pump house (1150)	1950-2018	886	
				Lukulu (2030)			
Luena (Angola)	19,924	Zambezi					
Lumbala	24,183	Zambezi					
Kabompo	72,068	491.0		Kabompo Boma* (1650)	2000-2008	165	83
					1958-2019	273	
				Watopa (1950)			
Lungwebungo	47,071	754.1					375
Makondu	6,278	Zambezi					
Dongwe	20,911	Kabompo					
West Lunga	12,031	Kapombo					
Mwafwe	10,581	Kabompo					
Luena (Zambia)	21,641	Zambezi					
Kafue	102,714	739,1	Discharge, stage	Chilenga (4350)	1962-2007	153	180
					1953-2005	162	
				M'Swebi (4435)	1959-2007	147	
					1973-2008	231	
				Lubungu (4450)			
				Hook Pontoon (4670)			
Lunga	24,517	Kafue		Chifumpa Pontoon (4560)	1959-2007	87	
Lukanga	13,925	Kafue					
Lufupa	10,451	Kafue					
Luswishi	9,470	Kafue					
Luangwa	149,523	989.4	Discharge, stage	Great East Rd. Bridge (5940)	1948-2002	168	230
Lunsemfwa	44,356	Luangwa					
Lukusashi	14,950	Lunsemfwa					
Mwomboshi	8,939	Luangwa					

We note a discrepancy in the discharge record at Kabompo Boma, in the Upper Zambezi (**Figure A. 1**). In the early 1990s, the annual minimum flow is below 100 m^3/s. Post-2000 there is a shift in the dry season flow. The same shift is seen in the water level records, suggesting the change may be due to a change in the reference height. Using the same rating curve results in the shift observed in the hydrograph. Closer inspection, reveals a bias in stage of 65 cm

between the pre- and post-2000 records. Comparison with the closest downstream station, Watopa, confirms the discrepancy. We therefore apply a bias correction to the post-2000 stage records and calculate the discharge using the station rating curve. The resulting corrected discharge was used to calibrate the model at Kabompo Boma.

Appendix B – Performance of the hydrological model

Performance measures used to calibrate the hydrological model include evaluation of the flow duration curve, using the performance measure presented in Westerberg et al. (2011) and the RMSD of the daily discharge climatology (Kittel et al., 2018). Values between 0 and 1 are deemed acceptable – perfect prediction yields scores of respectively 1 and 0. In addition to these two performance measures, we calculate the non-parametric version of the Kling-Gupta Efficiency measure as proposed by Pool et al. (2018).

Table B. 1 Summary of calibration setup of the rainfall-runoff model and performance statistics at the calibration and validation stations

	Calibration zones	Calibration and validation stations	RMSD of discharge climatology	Flow duration curve	Non-parametric KGE
Upper Zambezi	1. Low slope, dominant forest cover 2. Low slope, land cover mosaic 3. High slope, dominant forest cover	1. Watopa (C) 2. Chavuma (C) 3. Kabompo Boma (C)	1. 0.63 2. 1.05 3. 0.79	1. 0.12 2. 0.21 3. 0.15	1. 0.82 2. 0.74 3. 0.84
Kafue	1. Low slope, forest cover > 75% 2. Low slope, land cover mosaic 3. High slope, forest and shrub mosaic 4. High slope, forest cover > 80%	1. Lubungu (C) 2. Hook Pontoon (C) 3. Chilenga (C) 4. Chifumpa Pontoon (C)	1. 1.47 2. 0.83 3. 0.57 4. 1.64	1. 0.08 2. -0.36 3. -1.04 4. -0.72	1. 0.88 2. 0.87 3. 0.90 4. 0.74
Luangwa	1. High cover, forest mosaic	1. Great East Rd. Bridge (C)	1. 0.58	1. 0.002	1. 0.37

Appendix C – Steady-state solver with lateral inflow

The Saint-Venant equations express the mass balance and momentum balance equations for gradually varied one-dimensional flow in an open channel

$$\frac{\partial A}{dt} + \frac{dQ}{dx} = q \qquad (C.1)$$

$$\frac{\partial Q}{\partial t} + \frac{\partial}{\partial x}\left(\frac{\beta Q^2}{A}\right) + gA\frac{\partial h}{\partial x} - gA\left(S_0 - S_f\right) = 0 \qquad (C.2)$$

If we assume steady flow, i.e. constant Q, and no lateral inflow, the mass balance equation (Eq. C.1) becomes equal to the lateral inflow and Saint-Venant equations simplify to

$$\frac{dh}{dx} - \frac{Q^2}{gA^3}\frac{dA}{dx} - S_0 + \frac{Q^2}{K^2} = 0 \qquad (C.3)$$

By taking the partial derivative of the area relative to the chainage and width, and expanding the first term, Eq. C.2 becomes:

$$\left(1 - \frac{Q^2}{gA^3}\frac{\partial A}{\partial h}\right)\frac{dh}{dx} - \frac{Q^2}{gA^3}\frac{\partial A}{\partial x} - S_0 + \frac{Q^2}{K^2} = 0 \qquad (C.4)$$

Isolating the change in depth over the chainage gives the general form of the equation to solve

$$\frac{dh}{dx} = \frac{\left(\frac{Q^2}{gA^3}\frac{\partial A}{\partial x} + S_0 - \frac{Q^2}{K^2}\right)}{\left(1 - \frac{Q^2}{gA^3}\frac{\partial A}{\partial h}\right)}$$

$$\frac{dh}{dx} = RHS\left(x, h(x)\right) \qquad (C.5)$$

Where RHS (Right Hand Side) is the collection of terms not containing the derivative of the depth with respect to the chainage. We can replace $\frac{\partial A}{\partial h}$ and $\frac{\partial A}{\partial x}$ with channel properties. For a rectangular channel with variable width $w = w(x)$

$$\frac{dh}{dx} = \frac{\left(\frac{Q^2}{gA^3}\frac{dw}{dx} + S_0 - \frac{Q^2}{K^2}\right)}{\left(1 - \frac{Q^2}{gA^3}b\right)} \qquad (C.6)$$

If we apply this method to larger river networks, there will be lateral inflow, q, at certain points. Therefore, we must take into account

$$\frac{d}{dx}\frac{Q^2}{A} = \frac{A\frac{dQ^2}{dx} - Q^2\frac{dA}{dx}}{A^2} \qquad (C.7)$$

$$\frac{dQ^2}{dx} = \frac{d(Q^2)}{dQ}\frac{dQ}{dx} = 2Q \times q \qquad (C.8)$$

Eq. 10 becomes

$$\frac{dh}{dx} = \frac{\left(\frac{Q^2}{gA^3}\frac{\partial A}{\partial x} + S_0 - \frac{Q^2}{K^2} + \frac{2Q \times q}{gA^2}\right)}{\left(1 - \frac{Q^2}{gA^3}\frac{\partial A}{\partial h}\right)}$$

$$\frac{dh}{dx} = RHS\left(x, h(x)\right) \qquad (C.9)$$

Figure 1 Study area and in-situ gauging stations. Calibration is performed for the five highlighted reaches (Lungwebungo, Kabompo, Upper Zambezi, Kafue and Luangwa).

Figure 2 Selection of CryoSat-2 observations in the Zambezi. Left: longitudinal profile of each studied river reach, right: illustration of the outlier filtering process for a subset of each reach.

Figure 3 Top: Simulated against synthetic water level (the calibrated bed elevation is subtracted) for the six experiments. Bottom: Retrieval of synthetic Manning's roughness, n (left) and offset from the initial datum guess (right) by the model. The black crosses indicate the chainage of the synthetic observations consistent with the CryoSat-2 observation density.

Figure 4 Top: FAST sensitivity analysis of the synthetic calibration test with 20 cm standard deviation; the parameters are numbered from downstream to upstream cross-sections. Bottom: Sampling pattern and model performance during calibration at six randomly selected cross-sections. Cross-section numbering is from downstream to upstream. The objective is lowered during calibration.

Figure 5 Calibrated longitudinal profile of the bed elevation and the WSE simulated by the steady-state solver for the five subreaches in the Zambezi – the calibrated WSE is computed using the discharge of the corresponding day of observation by CryoSat-2 assuming steady-state.

Figure 6 WSE at in-situ stations Chavuma (Upper Zambezi – top row) and Watopa (Kabompo – middle row) and simulated by LISFLOOD-FP and Sentinel-3 WSE versus simulated WSE by LISFLOOD-FP at Sentinel-3 VS (bottom row). The shaded area represents the expected uncertainty of Sentinel-3 of up to 50 cm.

Figure 7 Selected calibrated river cross-sections versus MERIT DEM bed and bank elevations (left) and calibrated bed elevation versus the MERIT DEM river surface longitudinal profiles (right).

Figure A. 1 Water level at Kabompa Boma over the years of observation with at least 250 days of record and discharge record before and after record. Watopa is the next downstream station. The corrected minimum discharge is coherent when projecting the water level onto the pre-2000 datum.

753

Figure 1.

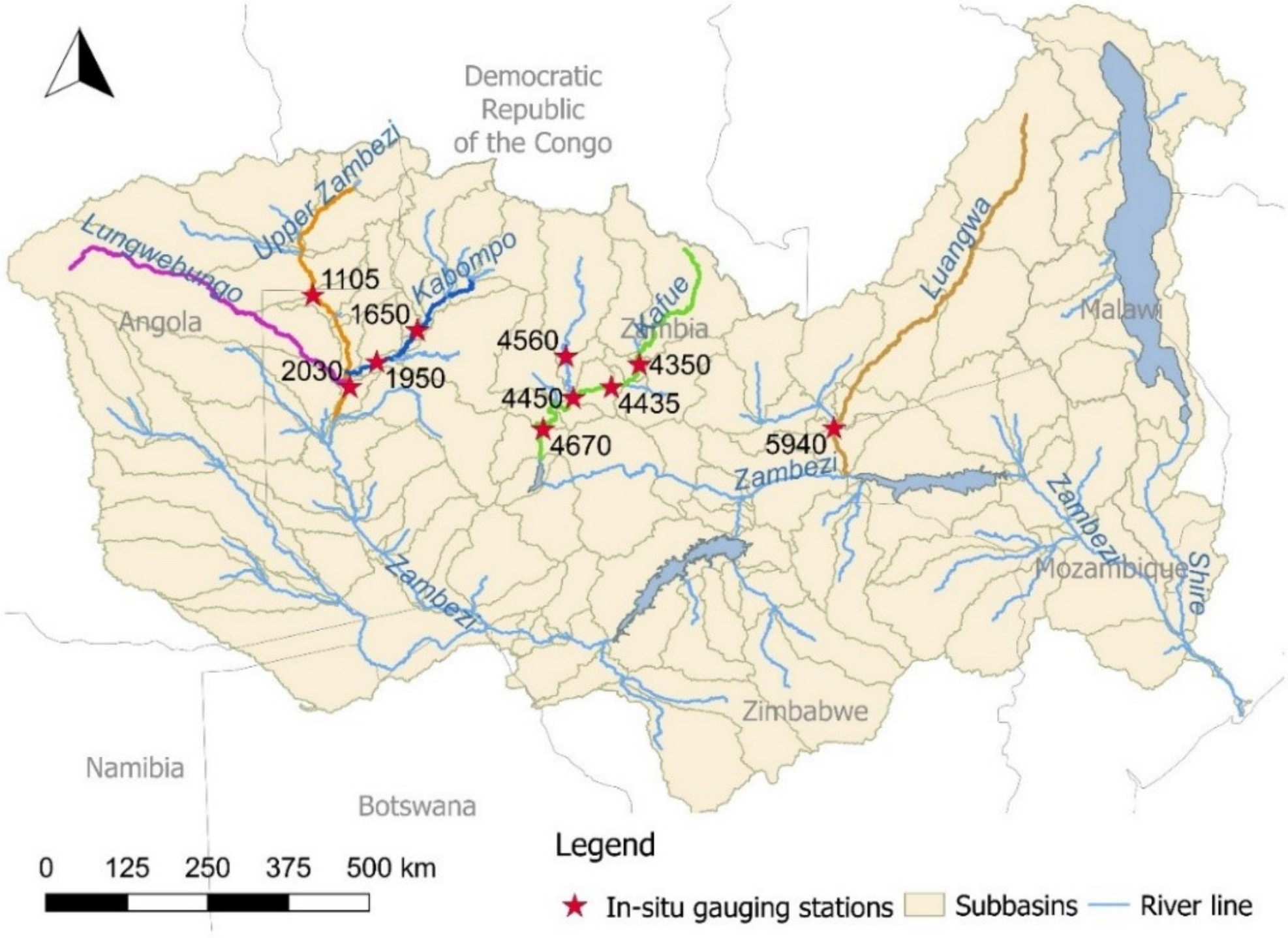
Democratic
Republic
of the Congo
Upper Zambezi
Lungwebungo
Kabompo
Kafue
Luangwa
Angola
Zambia
Malawi
1105
1650
2030
1950
4560
4350
4450
4435
4670
5940
Zambezi
Zambezi
Mozambique
Shire
Zimbabwe
Namibia
Botswana
0 125 250 375 500 km
Legend
In-situ gauging stations
Subbasins
River line

Figure 2.

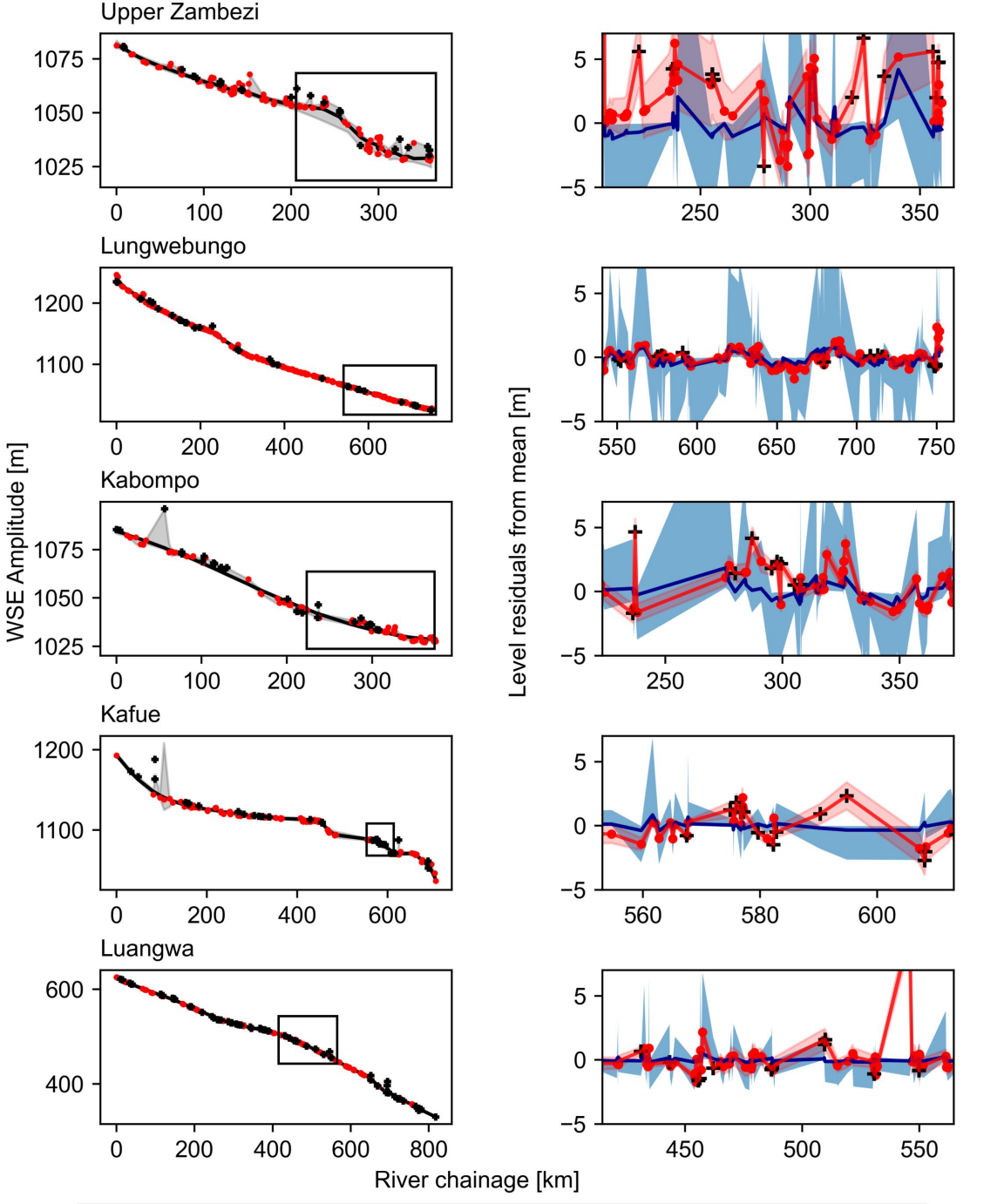
Upper Zambezi
Lungwebungo
Kabompo
Kafue
Luangwa
WSE Amplitude [m]
Level residuals from mean [m]
River chainage [km]
Predicted residuals
Mean expected residual
CryoSat-2 residuals
CryoSat-2 observations post-outlier filtering
Outliers
Spline curves
Median spline curve

Figure 3.

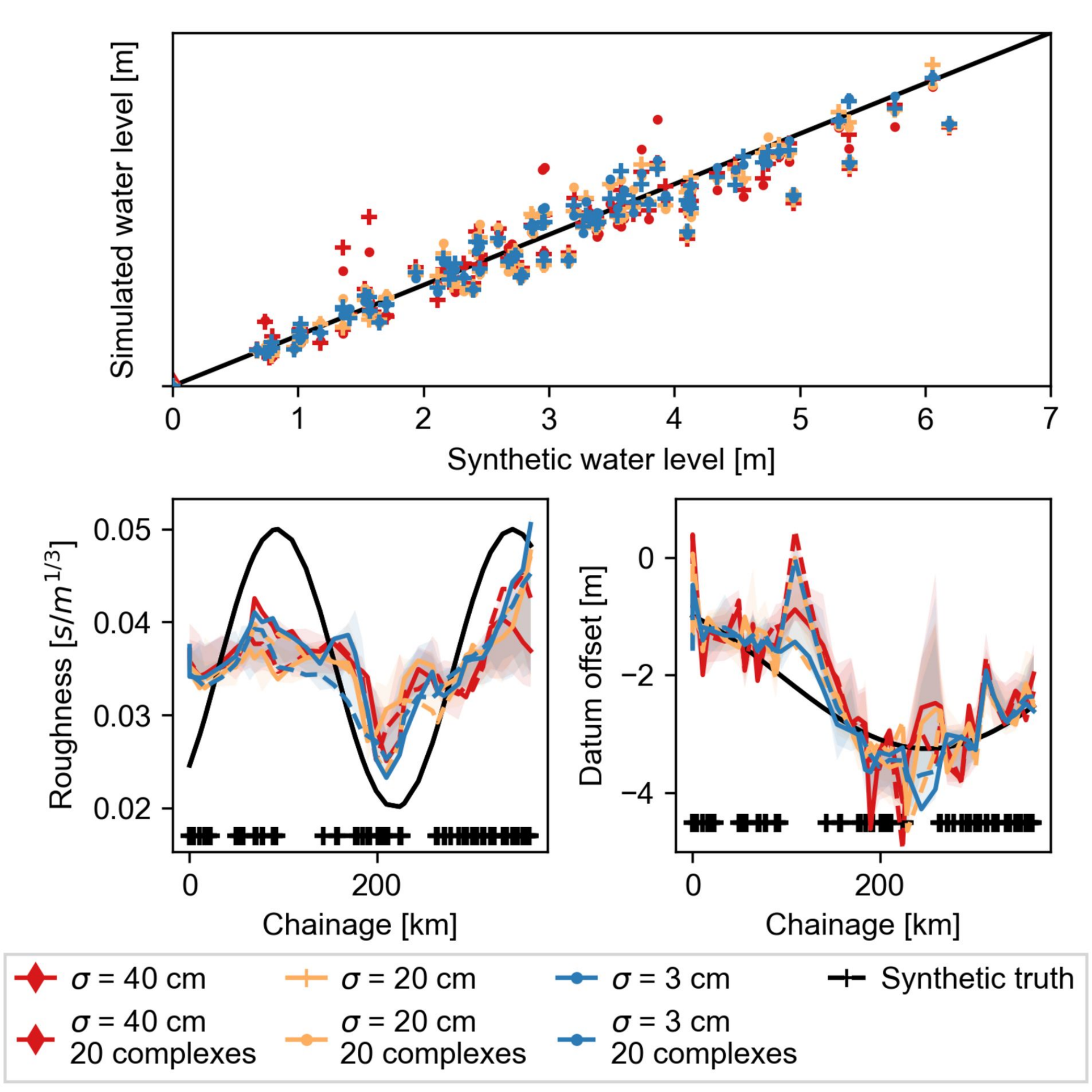
Simulated water level [m]
0
1
2
3
4
5
6
7
Synthetic water level [m]
Roughness [$s/m^{1/3}$]
0.05
0.04
0.03
0.02
0
200
Chainage [km]
Datum offset [m]
0
−2
−4
0
200
Chainage [km]
σ = 40 cm
σ = 20 cm
σ = 3 cm
Synthetic truth
σ = 40 cm
20 complexes
σ = 20 cm
20 complexes
σ = 3 cm
20 complexes

Figure 4.

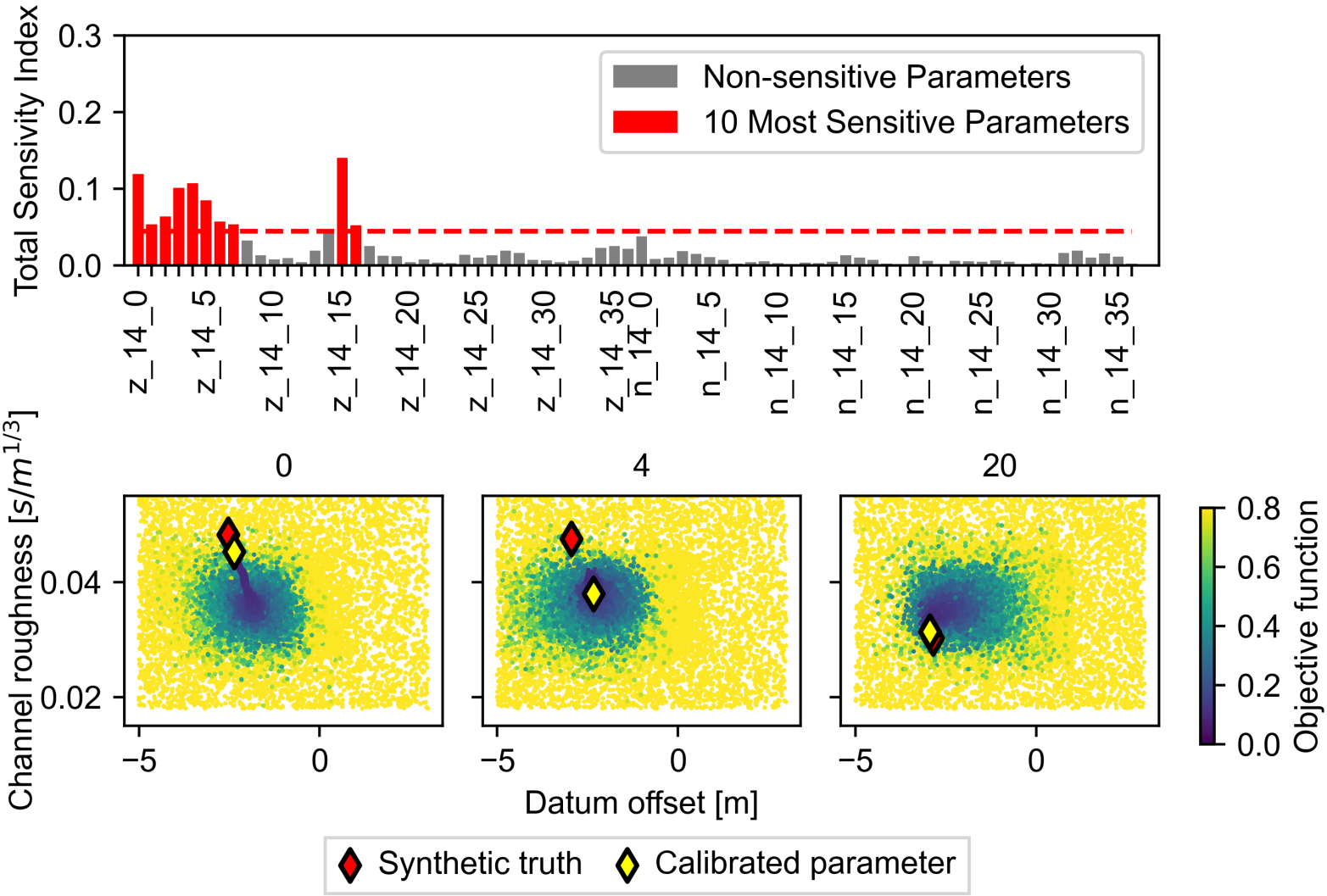
Total Sensivity Index
0.3
0.2
0.1
0.0
Non-sensitive Parameters
10 Most Sensitive Parameters
z_14_0
z_14_5
z_14_10
z_14_15
z_14_20
z_14_25
z_14_30
z_14_35
n_14_0
n_14_5
n_14_10
n_14_15
n_14_20
n_14_25
n_14_30
n_14_35
0
4
20
Channel roughness [s/m^1/3]
0.04
0.02
−5
0
Datum offset [m]
0.8
0.6
0.4
0.2
0.0
Objective function
Synthetic truth
Calibrated parameter

Figure 5.

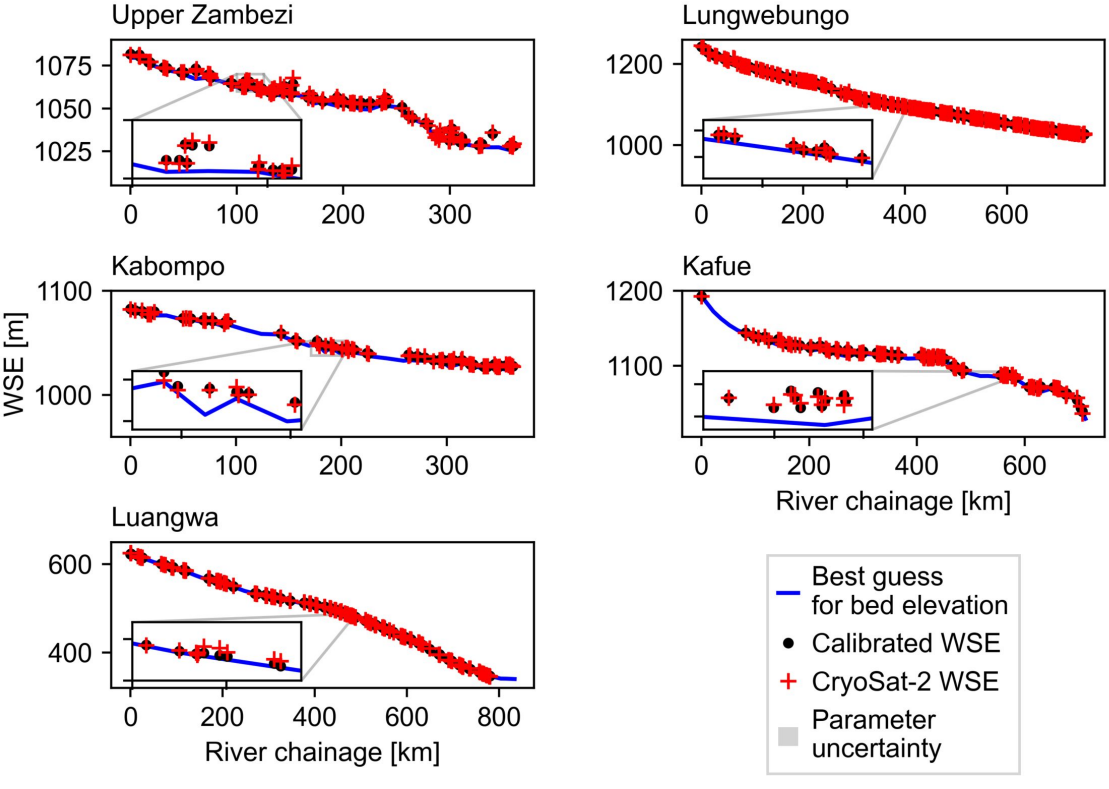
Upper Zambezi
Lungwebungo
Kabompo
Kafue
Luangwa
WSE [m]
River chainage [km]
Best guess for bed elevation
Calibrated WSE
CryoSat-2 WSE
Parameter uncertainty

Figure 6.

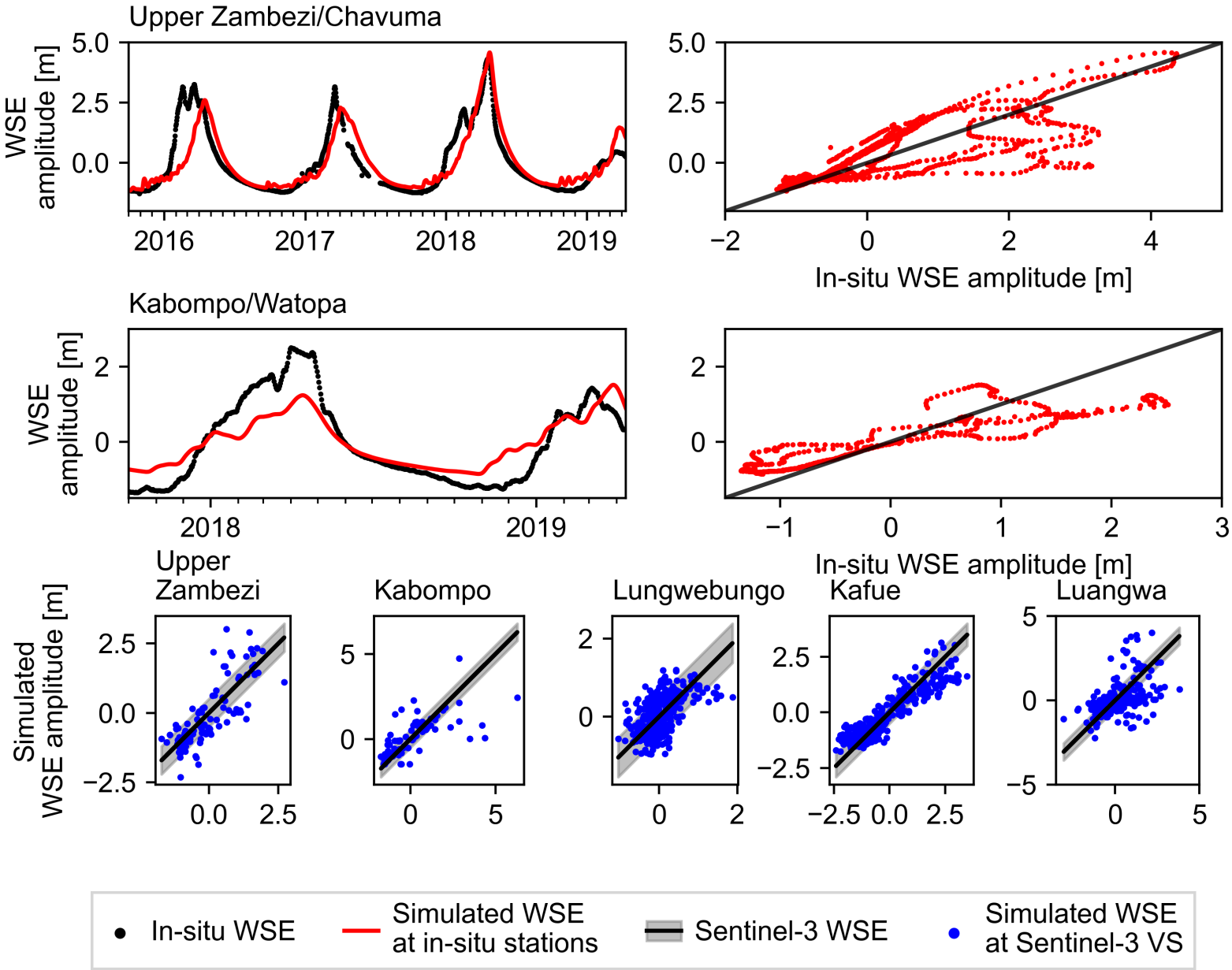
Upper Zambezi/Chavuma
WSE amplitude [m]
5.0
2.5
0.0
2016
2017
2018
2019
−2
0
2
4
In-situ WSE amplitude [m]
Kabompo/Watopa
2
0
2018
2019
−1
1
3
Upper Zambezi
Kabompo
Lungwebungo
Kafue
Luangwa
Simulated WSE amplitude [m]
In-situ WSE
Simulated WSE at in-situ stations
Sentinel-3 WSE
Simulated WSE at Sentinel-3 VS

Figure 7.

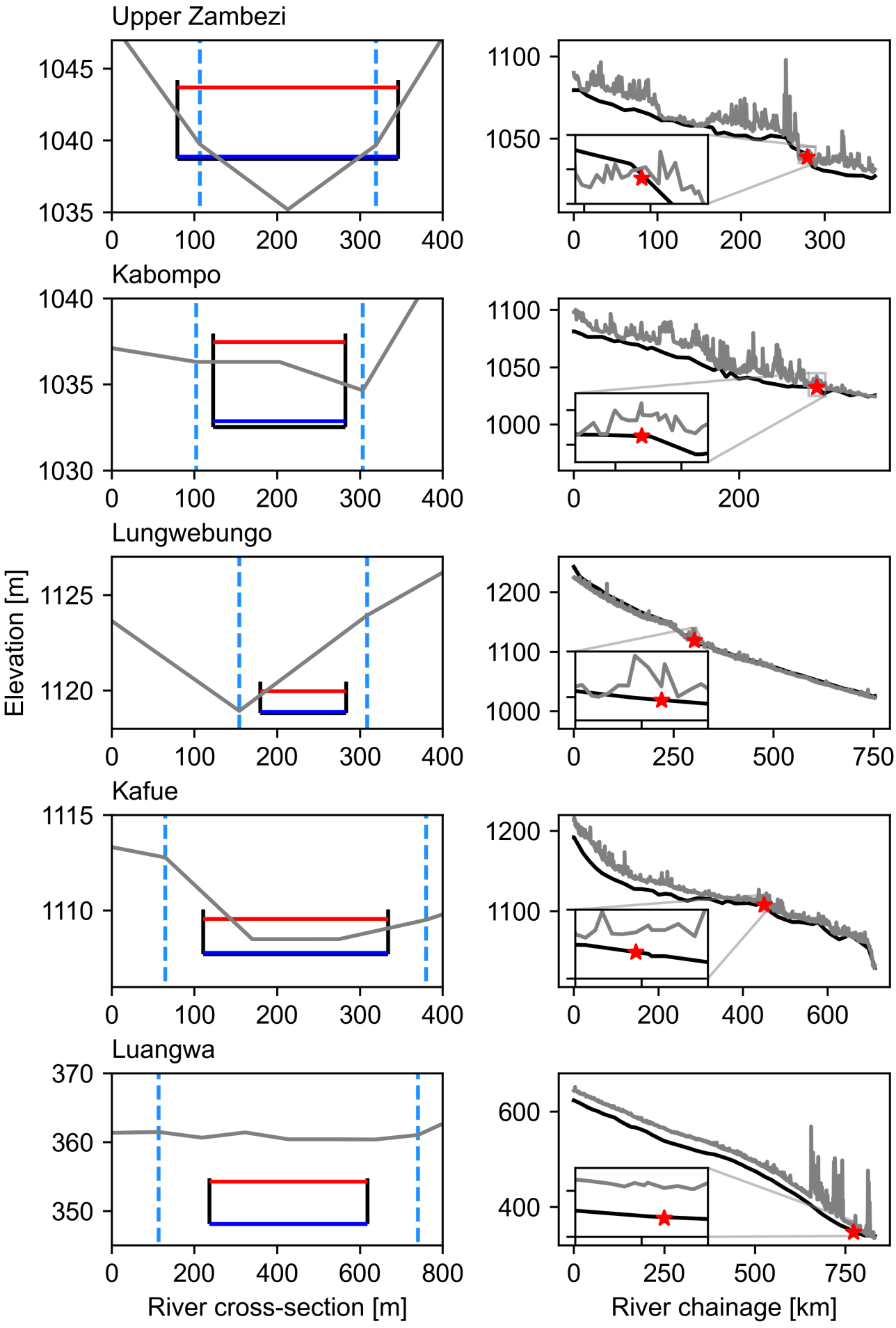
Upper Zambezi
Kabompo
Lungwebungo
Kafue
Luangwa
Elevation [m]
River cross-section [m]
River chainage [km]
DEM elevation
Calibrated elevation
Low flow
High flow
Cross-sections
River extent

Figure A1.

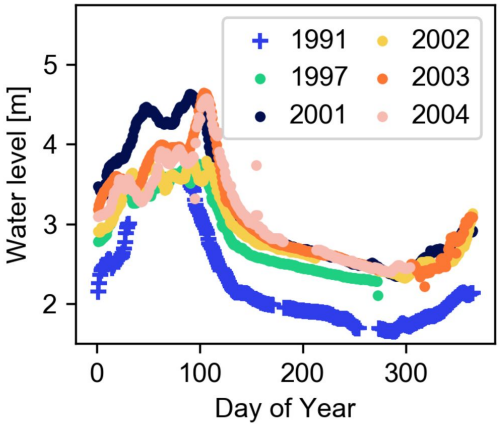
1991
1997
2001
2002
2003
2004
Water level [m]
Day of Year
0
100
200
300
2
3
4
5

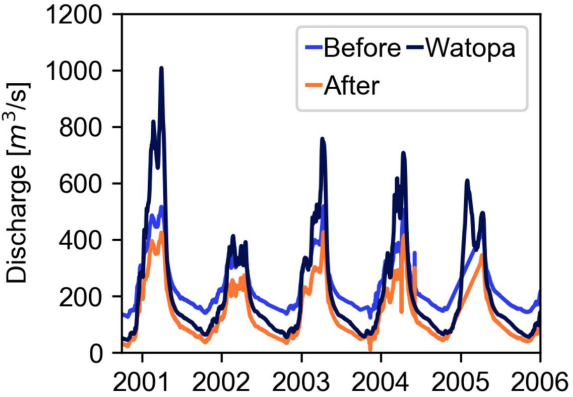
Before
Watopa
After
Discharge [m^3/s]
0
200
400
600
800
1000
1200
2001
2002
2003
2004
2005
2006